

# Hydrodynamic shielding in radiative multicloud outflows within multiphase galactic winds

A. S. Villares<sup>1</sup>\*, W. E. Banda-Barragán<sup>1,2</sup>†, and C. Rojas<sup>1</sup>

<sup>1</sup>*Escuela de Ciencias Físicas y Nanotecnología, Universidad Yachay Tech, Hacienda San José S/N, 100119 Urcuquí, Ecuador*

<sup>2</sup>*Hamburger Sternwarte, University of Hamburg, Gojenbergsweg 112, 21029 Hamburg, Germany*

Accepted XXX. Received YYY; in original form ZZZ

## ABSTRACT

Galactic winds are multi-phase outflows of energy and matter leaving star-forming galaxies. Emission and absorption line observations reveal that these winds are multiphase, hosting populations of cold gas clouds. The detection of such cold gas at significant distances from the centres of galaxies is a mystery given the ease with which such cold clouds can be disrupted. Numerical simulations of cold gas streams are essential to comprehend the underlying physical processes behind cold gas survival. Here we report a suite of 3D hydrodynamical simulations of supersonic winds interacting with a multi-cloud system. We study how radiative cooling and different cloud separation distances influence the outflow evolution. In agreement with single-cloud models, we find that the lifetime of dense and cold material in radiative clouds is longer than in their adiabatic counterparts. This is due to the condensation of warm mixed gas, which effectively sustains dense gas along the flow. In addition, we find that when clouds are further apart, they are more likely to generate dynamical instabilities, leading to higher degrees of mixing and dense gas destruction. Conversely, when clouds are closer, the condensation mechanism is particularly important owing to hydrodynamic shielding, which helps to maintain higher percentages of cold material as the cloud separation distance becomes smaller. The velocity of cloud material decreases as the cloud separation distance decreases, as this arrangement triggers the generation of large column densities. Hydrodynamic shielding in radiative multicloud outflows is thus found to be effective in maintaining cold dense gas for extended periods of time.

**Key words:** Galaxy: halo – galaxies: starburst – methods: numerical

## 1 INTRODUCTION

Galactic winds are complex, multifaceted outflows of matter and energy that arise in star-forming galaxies (see a recent review by Faucher-Giguère & Oh 2023). These winds are made of molecular, atomic, and ionised components, which despite having specific densities and temperatures, coexist along the outflow (e.g., see Di Teodoro et al. 2020; Ponti et al. 2021; Veena et al. 2023 for the nuclear wind in our Galaxy, and Westmoquette et al. 2008; Veilleux et al. 2021; Li et al. 2022; Reichardt Chu et al. 2022; McPherson et al. 2023; Levy et al. 2023 for winds in starburst galaxies). Galactic winds are of great interest because they are one of the main mechanisms by which galaxies lose gas and metals, which in turn has a significant impact on how galaxies evolve (Roberts-Borsani et al. 2020; Veilleux et al. 2020). Emission- and (quasar) absorption-line observations of star-forming galaxies, particularly starburst galaxies, reveal the presence of multiphase outflows within galactic winds (see a review by Rupke 2018), in which a cold, dense gas component is embedded with much hotter and more diffuse gas phases (e.g. Shopbell & Bland-Hawthorn 1998; Tripp et al. 2011; Pfuhl et al. 2015; Teodoro et al. 2018; Salak et al. 2018; Rubin et al. 2022).

As they propagate outwards, galactic winds, launched by stellar feedback processes, encounter a diverse range of clumps with varying sizes in the interstellar and the circumgalactic media (see Strickland & Stevens 2000; Cooper et al. 2008; Schneider et al. 2020 for examples of simulations). Interstellar clumps are typically constituted by dense gas and dust clouds. The interaction between diffuse winds and these clouds results in significant alterations in the physical and chemical properties of both the hot winds and the cold clouds (see Gronke et al. 2022; Abruzzo et al. 2022; Pittard 2022; Jung et al. 2023 for recent simulation work). For example, when the outflowing material interacts with dense clouds, the ram pressure exerted by the wind material compresses the clouds, leading to their disruption (see e.g. Klein et al. 1994; Brüggen & Scannapieco 2016; Banda-Barragán et al. 2019). Moreover, the net force that results from the momentum transfer of the wind material to clouds can cause acceleration of the clouds (see Fragile et al. 2004; Cottle et al. 2020). This process acts upon the upstream side of the cloud, pushing dense material downstream and leading to its fragmentation (Gregori et al. 2000; Schneider & Robertson 2017; McCourt et al. 2018).

Considering the significance of galactic winds for the ecology of the interstellar medium (ISM) and the circumgalactic medium (CGM), and for the global evolution of galaxies, it is crucial to gain a comprehensive understanding of the underlying physical processes that shape them (Tumlinson et al. 2011). Numerical simulations are

\* E-mail: andres.villares@yachaytech.edu.ec (ASV)

† E-mail: wbandabarragan@gmail.com (WEBB)

essential tools to better understand the observations and the physical characteristics of the gas in such outflows. Indeed, a long history of numerical simulation studies of galactic winds exists. These studies encompass a wide range of hydrodynamic and magnetohydrodynamic models with different resolutions and domain sizes. Depending on the length scales that are targeted by the models, simulations can be classified in wind-cloud (e.g., Schneider & Robertson 2017; Sparre et al. 2020), wind-multicloud (e.g., Aluzas et al. 2012; Banda-Barragán et al. 2020), wind-launching (e.g., Choi et al. 2022; Rathjen et al. 2023), and disc-wind (e.g., Schneider et al. 2020; Zhang et al. 2021) models.

Wind-cloud simulations have demonstrated that the hot wind has the ability to erode and remove material from the clouds, eventually leading to their destruction via dynamical instabilities (see Nakamura et al. 2006; Banda-Barragán et al. 2016). These models show that clouds can be easily destroyed in galactic wind environments. This occurs not only in adiabatic or inefficient-cooling scenarios (Pittard & Parkin 2016; Goldsmith & Pittard 2017), but also in models for which cooling is important (i.e. models for which the cooling time is smaller than the cloud-crushing time, e.g. Cooper et al. 2009; Schneider & Robertson 2017). The fact that clouds are destroyed (before they can reach high speeds) over a wide range of initial conditions has posed some tension between simulations and astronomical observations (Zhang et al. 2017), which show the co-existence of cold clouds at very large distances from the galactic planes (e.g., see Borthakur et al. 2015; Rubin et al. 2022; Tchernyshov et al. 2022 and a review by Rupke 2018). Recently, however, Gronke & Oh (2018, 2020) identified a region of the parameter space of wind-cloud interactions that facilitate cloud survival and even promote dense-gas mass growth. When the cooling time of the mixed warm gas (which forms via cloud erosion) is smaller than the cloud-crushing time, fast-moving cold gas reforms from the mixed phase (see also Marinacci et al. 2010; Li et al. 2020; Kanjilal et al. 2021).

While small-scale wind-cloud simulations have played an important role in understanding the entrainment of cold gas in hot ambient winds, they are still idealised models as they consider clouds as isolated entities. In reality, ISM and CGM clouds reside in multi-phase outflows in which inter-cloud interactions are also expected (e.g. see McClure-Griffiths et al. 2013, 2018; Veena et al. 2023 for our Galaxy's galactic wind, where individual outflowing clouds can be somewhat resolved). Can such interactions help explain the presence of dense cold gas in galactic winds? As we show in this paper, the answer is yes and hydrodynamic shielding is responsible for aiding dense gas survival. Hydrodynamic shielding is the process by which multiple clouds along a gas stream mutually protect each other from disruption via drag forces. Previous wind-multicloud simulations of groups of adiabatic clouds placed along a stream or part of turbulent density fields have demonstrated that hydrodynamical shielding can be an effective mechanism for extending their lifespan (see Forbes & Lin 2019; Banda-Barragán et al. 2020; Aluzas et al. 2012). In particular, (Forbes & Lin 2019) studied adiabatic wind-multicloud systems with subsonic and transonic winds, showing that clouds can shield themselves provided that the separation distance between them is initially small.

The effects of hydrodynamic shielding has also been spotted in adiabatic simulations by (Aluzas et al. 2012; Banda-Barragán et al. 2020) in the form of warm shells of gas that result from inter-cloud interactions. Radiative wind-multicloud simulations (e.g. (Banda-Barragán et al. 2021)), large-scale wind-launching models (e.g. Kim et al. 2020), and disc-wind simulations (e.g. Schneider et al. 2018) also capture the overall effects of inter-cloud interactions, but the numerical resolution and the complexity of the resulting outflows

makes it hard to isolate the effects of hydrodynamic shielding in all these models. In addition, radiative wind-multicloud scenarios with supersonic winds have not been characterised before. Thus, in this paper we assess the ability of systems of identical clouds, travelling along a straight trajectory with an initial separation distance ( $\delta$ , in cloud radius units) between them, to protect themselves (i.e. show signs of hydrodynamic shielding) against hydrodynamic drag and dynamical instabilities arising from their interactions with a hot supersonic wind gas. We explore the differences that arise when radiative cooling and supersonic winds are included in the simulations, compared to their subsonic and adiabatic counterparts.

This paper is structured as follows: Section 2 outlines the methodology and initial conditions employed in our simulations, including the description of the software and computational tools used for simulations and data analysis. Section 3 presents the results obtained, provides a comprehensive discussion on hydrodynamic shielding, and compares them to previous studies. Section 4 discusses the effects of numerical resolution while also highlighting the limitations of our work. Finally, Section 5 summarises the key findings of this paper and provides final remarks.

## 2 METHODS AND SIMULATIONS

### 2.1 Simulation code

We investigate the interaction between streams of dense gas clouds embedded in a diffuse galactic wind. Our simulations were conducted using the PLUTO v4.3 code (Mignone et al. 2007). The simulations were carried out by simultaneously solving the ideal hydrodynamic (HD) equations in a three-dimensional Cartesian coordinate system ( $X, Y, Z$ ). The mass, momentum, and energy conservation laws are:

$$\frac{\partial \rho}{\partial t} + \nabla \cdot [\rho \mathbf{v}] = 0, \quad (1)$$

$$\frac{\partial [\rho \mathbf{v}]}{\partial t} + \nabla \cdot [\rho \mathbf{v} \mathbf{v} + \mathbf{I} \mathbf{P}] = 0, \quad (2)$$

$$\frac{\partial E}{\partial t} + \nabla \cdot [(E + P)\mathbf{v}] = \Lambda, \quad (3)$$

where  $\rho = \mu m_u n$  is the mass density,  $\mu$  is the mean particle mass,  $m_u$  is the atomic mass unit,  $n$  is the gas number density,  $\mathbf{v}$  is the velocity,  $P = (\gamma - 1)\rho\epsilon$  is the ideal gas thermal pressure,  $\gamma = \frac{5}{3}$  is the polytropic index,  $\epsilon$  represents the specific internal energy of the gas, and  $\Lambda$  is the volumetric cooling rate. In addition, we include the additional advection equation of the form:

$$\frac{\partial \rho C}{\partial t} + \nabla \cdot [\rho C \mathbf{v}] = 0, \quad (4)$$

where  $C$  is a Lagrangian scalar, which we used to track the evolution of gas initially contained in cloud material, i.e.,  $C = 1$  for the gas inside the multi-cloud system and  $C = 0$  everywhere else.

The simulations were performed using the HLLC approximate Riemann solver (Toro et al. 1994), jointly with a third-order Runge-Kutta method (RK3) as the time-marching algorithm and a second-order parabolic method for spatial reconstruction. Together these algorithms constitute a robust numerical scheme that adequately captures shocks and discontinuities in compressible flows (see Mignone 2014) and provides a good balance between accuracy and computational cost. Also, to ensure the stability of the numerical simulations, we set the Courant-Friedrichs-Lowy (CFL) number to 0.33.

## 2.2 Computational set-up

Our study involves the simulation of an idealised two-phase medium, composed of spherical cold clouds and a hot ambient wind (see Figure 1). Following (Forbes & Lin 2019), the clouds are arranged along a stream, surrounded by a hot supersonic wind with a uniform velocity field pointing in the  $Y$  direction. The simulation domain is a rectangular prism with a  $1 : 4 : 1$  aspect ratio for the  $X : Y : Z$  axes. In physical units, the domain has a volume of  $(100 \times 400 \times 100) \text{ pc}^3$ . To keep all the cloud gas inside the computational domain during the entire duration of the simulations and prevent biases due to material leaving it, we set up periodic boundary conditions on all sides of the computational domain.

## 2.3 Models

This study comprises a total of 20 models aimed at investigating the impact of hydrodynamic shielding in a multicloud gas stream (see Table 1). All simulations cover a time-scale of  $t_{\text{sim}} \sim 5 \text{ Myr}$ , and include spherical clouds with identical radii  $r_{\text{cl}} = 6.25 \text{ pc}$ , number density  $n_{\text{cl}} = 1.11 \times 10^{-4} \text{ g cm}^{-3}$ , and temperature  $T_{\text{cl}} = 10^4 \text{ K}$ , placed in a row along the  $Y$  direction. Depending on the model, the centres of the clouds are separated by different distances,  $d_{\text{sep}}$ , which we report using a dimensionless parameter  $\delta = d_{\text{sep}}/r_{\text{cl}}$  (see column 8 of Table 1 and Forbes & Lin 2019). In all cases the wind properties are fixed according to the CC85 model (Chevalier & Clegg 1985) and assuming the multicloud systems are at distances of  $r^* \sim 2 \text{ kpc}$  from the central starburst (see Appendix A). Thus, the wind has a density of  $n_{\text{wind}} = 1.11 \times 10^{-6} \text{ g cm}^{-3}$ , temperature  $T_{\text{wind}} = 10^6 \text{ K}$  and Mach number  $M_{\text{wind}} = v_{\text{wind}}/c_{\text{wind}} = 3.5$ , where the wind speed is  $v_{\text{wind}} = 500 \text{ km s}^{-1}$  and its sound speed is  $c_{\text{wind}} = 143.8 \text{ km s}^{-1}$ . Initially, the cloud-to-wind density contrast is  $\chi = 10^2$ , and both the wind and the multicloud system are set in pressure equilibrium at  $P/k_b = 1 \times 10^4 \text{ K cm}^{-3}$ .

In terms of numerical resolution, we have standard-resolution models with  $(256 \times 1024 \times 256)$  cells with 16 cells covering a cloud radius ( $R_{16}$ ), high-resolution models with 32 cells covering a cloud radius ( $R_{32}$ ), and low-resolution models with 8 cells covering a cloud radius ( $R_8$ ). Our control adiabatic and radiative runs have  $\delta = 16$ . In the first part of the study (presented in Section 3.1), we compare our control runs to study the overall evolution of wind-multicloud systems and the effects of radiative cooling. In the second part of our study (presented in Section 3.2), we compare 5 adiabatic and 5 radiative numerical simulations at  $R_{16}$  with different cloud separation distances ( $\delta$ ) to study the effects of hydrodynamic shielding and how  $\delta$  influences the evolution of cold clouds. In the last part of the study (see Section 4), we contrast the evolution of 4 adiabatic and 4 radiative simulations with higher and lower resolutions to study numerical convergence in both scenarios.

## 2.4 Radiative cooling

We study adiabatic models ( $\Lambda = 0$  in equation 3) and radiative models ( $\Lambda = n^2 \tilde{\Lambda}$  in equation 3). In the latter, the cooling rates,  $\tilde{\Lambda}$ , are read and interpolated from a table (Teşileanu et al. 2008), pre-compiled using the CLOUDY code (Ferland et al. 1998) for a solar mix of atomic gas at redshift zero. To prevent gas from cooling below  $10^4 \text{ K}$ , we impose a cooling floor at that temperature. This approach mimics the effects of heating processes in the CGM below  $10^4 \text{ K}$ , and also allows us to compare our results with previous studies for which similar (e.g., Brüggen & Scannapieco 2016; Gronke & Oh 2018; Casavecchia et al. 2023) or lower (e.g., Schneider & Robertson

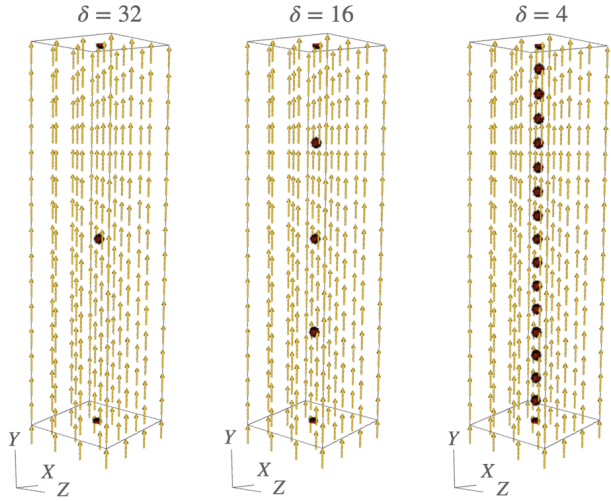


**Figure 1.** Three-dimensional setups of three of our wind-multicloud models featuring the initial positions of a collection of spherical clouds, each separated from one another by a uniform distance of  $\delta = 32, 16$ , and  $4$ , respectively. The arrows represent the uniform velocity field of the galactic wind.

2017; Banda-Barragán et al. 2021; Casavecchia et al. 2023) cooling floors are imposed.

## 2.5 Diagnostics

To study the evolution of a set of clouds in a wind-multicloud model, several diagnostics are calculated from the simulated data. Following (Banda-Barragán et al. 2016), the mass-weighted average of any variable  $\mathcal{G}$  is computed by:

$$\langle \mathcal{G} \rangle = \frac{\int \mathcal{G} \rho C dV}{M_{\text{cl}}} = \frac{\int \mathcal{G} \rho C dV}{\int \rho C dV}, \quad (5)$$

where  $V$  is the volume,  $C$  is the tracer of cloud material, and  $M_{\text{cl}}$  is the time-dependent cloud mass. In a similar way, the volume-weighted average of any variable  $\mathcal{F}$  is given by:

$$[\mathcal{F}] = \frac{\int \mathcal{F} C dV}{V_{\text{cl}}} = \frac{\int \mathcal{F} C dV}{\int C dV}, \quad (6)$$

where  $V_{\text{cl}}$  is the time-dependent cloud volume.

The degree of mixing between the cloud and the surrounding wind is defined as:

$$f_{\text{mix}} = \frac{\int \rho C^* dV}{M_{\text{cl},0}}, \quad (7)$$

where the numerator represents the mass of mixed gas with  $C^* = C$  when  $0.01 < C < 0.99$ , and  $M_{\text{cl},0}$  represents the mass of the cloud material at time  $t = 0$  (Xu & Stone 1995). Additionally, we define the dense-gas mass fraction (Heyer et al. 2022) as the ratio of cloud mass with densities greater than a threshold density,  $\rho_{\text{th}}$ , to the total cloud mass:

$$f_{\text{dense}} = \frac{M_{\text{cl}}(\rho_{\text{cl}} > \rho_{\text{th}})}{M_{\text{cl},0}}, \quad (8)$$

where  $\rho_{\text{th}} = \rho_{\text{cl},0}/2$  to focus on the cloud material with densities higher than half the initial cloud density. For comparison, we also

**Table 1.** Overview of the simulation parameters chosen for different models. Columns 1 and 2 respectively indicate the type of thermodynamic model and the numerical resolution in units of  $X$  number of cells per cloud radius with the standard notation, ( $R_x$ ). Columns 3, 4, 5, and 6 indicate the number of cells in the 3D domain, the size of the domain in physical units, the density contrast between the clouds and the wind, and the adiabatic index, respectively. Column 6 indicates the wind Mach number,  $M_{\text{wind}} = v_{\text{wind}}/c_{\text{wind}}$ . Columns 7 and 8 indicate the cooling floor and the initial separation distance between clouds given by the dimensionless parameter  $\delta = d_{\text{sep}}/r_{\text{cloud}}$ . The fixed parameters for all models include the cloud number density  $n_{\text{cl}} = 1.11 \times 10^{-4} \text{ g cm}^{-3}$ , cloud temperature  $T_{\text{cl}} = 10^4 \text{ K}$ , wind number density  $n_{\text{wind}} = 1.11 \times 10^{-6} \text{ g cm}^{-3}$ , wind temperature  $T_{\text{wind}} = 10^6 \text{ K}$ , wind speed  $v_{\text{wind}} = 500 \text{ km s}^{-1}$  and its sound speed  $c_{\text{wind}} = 143.8 \text{ km s}^{-1}$ .

| (1)<br>Model | (2)<br>Resolution | (3)<br>Number of cells | (4)<br>Computational domain [pc <sup>3</sup> ] | (5)<br>$\chi$ | (6)<br>$\gamma$ | (7)<br>$M_{\text{wind}}$ | (8)<br>Cooling floor | (9)<br>$\delta$     |
|--------------|-------------------|------------------------|--|---------------|-----------------|--------------------------|----------------------|---------------------|
| Adiabatic    | $R_{16}$          | (256 × 1024 × 256)     | (100 × 400 × 100)                              | $10^2$        | 5/3             | 3.5                      | -                    | 2, 4, 8, 16, 32, 64 |
| Radiative    | $R_{16}$          | (256 × 1024 × 256)     | (100 × 400 × 100)                              | $10^2$        | 5/3             | 3.5                      | $10^4$               | 2, 4, 8, 16, 32, 64 |
| Adiabatic    | $R_{32}$          | (512 × 2048 × 512)     | (100 × 400 × 100)                              | $10^2$        | 5/3             | 3.5                      | -                    | 8, 16               |
| Adiabatic    | $R_8$             | (128 × 512 × 128)      | (100 × 400 × 100)                              | $10^2$        | 5/3             | 3.5                      | -                    | 8, 16               |
| Radiative    | $R_{32}$          | (512 × 2048 × 512)     | (100 × 400 × 100)                              | $10^2$        | 5/3             | 3.5                      | $10^4$               | 8, 16               |
| Radiative    | $R_8$             | (128 × 512 × 128)      | (100 × 400 × 100)                              | $10^2$        | 5/3             | 3.5                      | $10^4$               | 8, 16               |

compute the mass of cold gas, which is defined as the mass of material whose temperature is below  $10 T_{\text{cl},0}$ , where  $T_{\text{cl},0}$  represents the initial temperature of the cloud:

$$f_{\text{cold}} = \frac{M_{\text{cl}}(T_{\text{cl}} < 10 T_{\text{cl},0})}{M_{\text{cl},0}}. \quad (9)$$

This fraction corresponds to a temperature in between the initial temperatures of the cloud and the wind (Forbes & Lin 2019), since the simulation is initialised in thermal pressure equilibrium with a density contrast of  $\chi = 10^2$ .

Finally, we introduce the concept of cloud-crossing time (Forbes & Lin 2019), which represents the duration for the flow around the cloud to cross one cloud radius. This is defined as follows:

$$t_{\text{cross}} = \frac{r_{\text{cl}}}{v_{\text{wind}}} = 0.012230501 \text{ Myr}, \quad (10)$$

where  $r_{\text{cl}}$  represents the radius of the cloud, while  $v_{\text{wind}}$  represents the initial relative velocity of the wind with respect to the cloud. The simulation time is then  $t_{\text{sim}} = 400 t_{\text{cross}}$ .

### 3 RESULTS

#### 3.1 Evolution of wind-multicloud systems

Figure 2 shows 2D slices at  $Z = 0$  of the gas number density. These panels correspond to our control adiabatic (top panel a) and radiative (bottom panel b) models with the standard separation distance,  $\delta = 16$ . The overall evolution of this pair of models, which is also relevant for the others, can be characterised by the following stages:

(i) **Shock formation:** In the first stage, the impact of the wind material on the front surfaces of the clouds produces internal shocks within them. The internal (refracted) shocks are accompanied by external (reflected) waves, which travel upstream. The reflected waves create bow shocks at the leading edges of the clouds, while the refracted shocks travel through the clouds. Due to pressure gradient forces and shock heating, which result from the initial impact, clouds start to accelerate and expand, stretching in the downstream direction (i.e. vertically along  $Y$ ). As the clouds expand, they start to undergo hydrodynamic disruption, resulting in the formation of filamentary tails. Such tails are turbulent and comprise mixed gas, which exhibits

densities and temperatures intermediate to that of the wind and the initial clouds.

(ii) **Hydrodynamic shielding:** In the second stage, a mixture of wind gas and upstream cloud material continues to flow downstream, enveloping downstream clouds. The downstream motion of the wind triggers interactions between the filamentary tails of the upstream clouds with the front edges of the downstream clouds. The presence of mixed gas in between the clouds reduces the drag forces to which they are subjected and provides hydrodynamic shielding to the downstream clouds. This process plays a crucial role in preserving the structural integrity of downstream cloud cores because it reduces cloud acceleration and thus delays the growth of Rayleigh-Taylor (RT) instabilities (at least to a certain degree). Clouds then effectively protect each other from disruption associated with drag forces and RT instabilities. Meanwhile, as the boundary conditions are periodic along  $Y$ , the turbulent tails of downstream clouds also interact with the upstream clouds. This interaction enhances the creation of a long gas stream of dense material (see the panels in middle column of Figure 2 for  $t = 1.1 \text{ Myr}$ ).

(iii) **KH shredding and mixing:** In the third stage, the degree of mass loss and mixing become dominant. Clouds steadily lose mass from their surface layers via stripping caused by Kelvin-Helmholtz (KH) instabilities. The growth time of KH instabilities in hydrodynamical models depends mainly on the density contrast between both media,  $\chi$ , and the relative velocity at the boundary layer, ( $v_{\text{wind}} - v_{\text{cl}}$ ). KH instabilities occur primarily at the sides of the clouds, where higher velocity shears exist, so hydrodynamic shielding has less impact on them than it has on RT instabilities. The swirling vortical motions associated with KH instabilities remove cloud material, which is carried downstream leading to the mixing of wind and cloud material. Shredding promotes acceleration as cloud cores become more diffuse owing to mass loss. The disruption process eventually forms long streamers of stripped gas that extend across the domain. The strength of the bow shock also decreases over time as the momentum transfer between the wind and the cloud takes place and results in cloud acceleration.

(iv) **RT break-up and disruption:** In the fourth stage, the clouds have undergone substantial mass loss as a result of KH shredding. Additionally, their acceleration has reached a level that is conducive to the growth of long-wavelength RT instabilities. The RT instabilities favour the formation of low-density wind gas bubbles and high-density spikes of cloud material at the front of each cloud. As

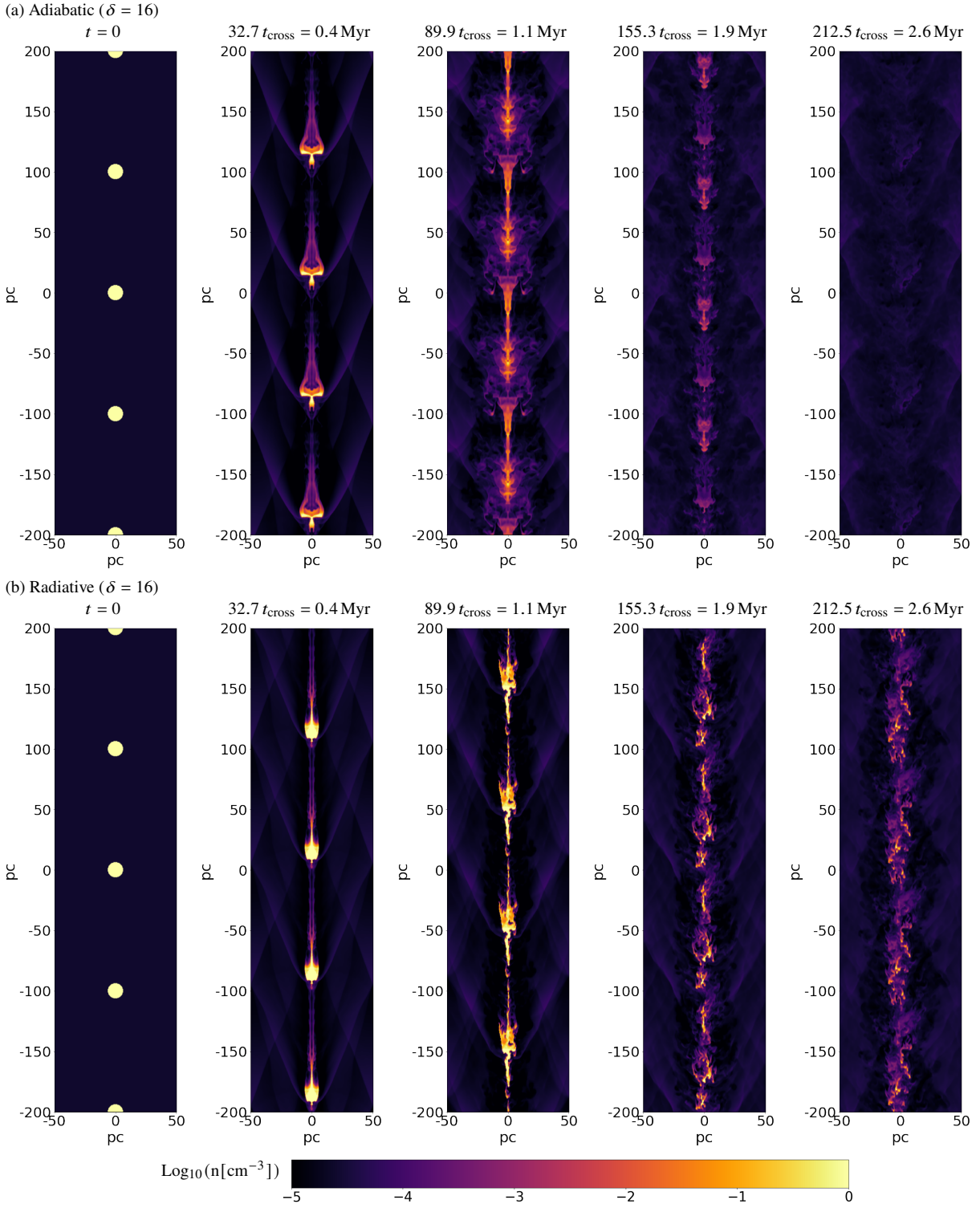


**Figure 2.** 2D slices at  $Z = 0$  of the gas number density in the adiabatic (top panel a) and radiative (bottom panel b) control models at five different times (shown in columns) throughout the simulation. The evolution of the models begins almost identically with the formation of a bow shock as the wind interacts with the front surface of each cloud. The subsequent injection of thermal energy in the adiabatic model increases the temperature of the cloud gas and contributes to the expansion and mixing of cloud and wind gas. Without radiative cooling, the cold gas in the adiabatic model is heated up and disrupted by instabilities much faster compared to that in the radiative model.

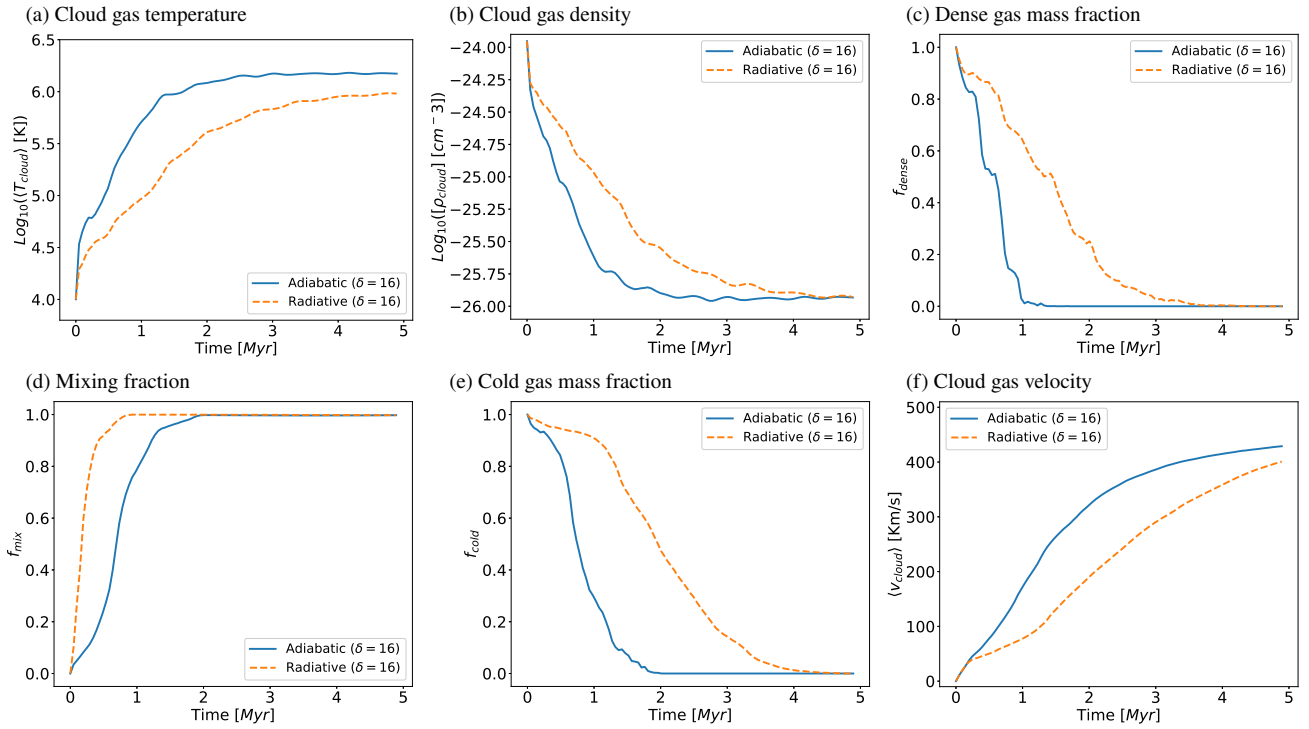


**Figure 3.** Time evolution of the mass-weighted average temperature (top left panel), mean density (top middle panel), dense gas mass fraction (top right panel), mixing fraction (bottom left panel), cold gas mass fraction (bottom middle panel), and mass-weighted average velocity (bottom right panel) of cloud material in the adiabatic and radiative  $\delta = 16$  models. The radiative model extends the lifetime of dense gas compared to the adiabatic model by enabling the replenishment of dense gas along the flow, which maintains temperatures lower than the ambient temperature. Adiabatic clouds mix due to KH and RT instabilities, while radiative clouds mix more efficiently due to turbulence and cooling-induced pressure gradients led by condensation. Mixing aids the survival of cold gas in the radiative model, as mixed cloud material can condense back into a colder and denser phase. Adiabatic clouds accelerate through direct momentum transfer, while radiative clouds cannot accelerate through direct momentum transfer due to their high column densities.

the cross-sectional area increases, RT instabilities grow, which results in the disruption of the main cloud cores. Cores break up into smaller clouplets. Some of these clouplets eventually dissolve into the background medium, acquiring high velocities close to the wind speed. Ultimately, it is RT perturbations that cause the destruction of clouds. Low-density bubbles rapidly penetrate the denser layers of the clouds, causing disruption to the remaining cloud filaments. The remaining clouds then fragment into several clouplets, which expand and mix further with the ambient gas. This process represents the final stage of cloud shredding and ultimately results in the complete destruction of the multi-cloud system.

It is important to remark that the break-up process can be accelerated or decelerated, depending on the inclusion or not of radiative cooling and on the initial separation distance,  $\delta$ , of the clouds. In particular, panel b in Figure 2 shows that radiative cooling can prolong the lifetime of dense gas in the multicloud system, but does not prevent disruption.

### 3.1.1 The role of radiative cooling

Comparing our two control models presented in Figure 2, it is apparent that their evolution begins almost identically. A bow shock is formed as the wind interacts with the front surface of each cloud. In the adiabatic model, the shock produced from the interaction between the wind and the clouds results in the compression of the cloud and the subsequent injection of thermal energy. This energy is then converted into heat, which not only increases the temperature of the

cloud (see Figure 3) but also contributes to the expansion and mixing of cloud and wind gas. Without an energy dissipation mechanism, dense gas is efficiently heated and disrupted by instabilities.

In contrast, radiative cooling removes the aforementioned thermal energy (injected by internal shocks) that would have been otherwise converted into heat. This prevents the pronounced increase in thermal pressure and temperature characteristic of adiabatic models. As a result, radiative cooling produces denser clouds where the cooled gas remains protected from instabilities, enveloped by a warm ( $T \sim 10^{4.5}$ K) radiative layer of mixed, medium-density gas. As a result, the most significant effect of the inclusion of radiative cooling is that dense gas exhibits a longer lifetime (see Figure 3).

Figure 3 shows the time evolution of the mass-weighted average temperature (see equation 5), the mean cloud density (see equation 5), and the dense gas mass fraction (see equation 8), all of cloud material, in our control adiabatic and radiative models. In the absence of radiative cooling, the adiabatic wind-multicloud system maintains its dense gas mass only until  $t \sim 1.2$  Myr while the radiative model still maintains  $\sim 60\%$  of dense material over the same time-scale. Eventually, at the end of the simulation time, both models lose all the dense material, but it is important to note that the radiative model prolongs the lifetime of dense gas at least three times compared to the adiabatic model. As cloud gas continues interacting with upstream clouds and the wind, it continues mixing, producing warm gas with temperatures  $T < 10^5$ K. This denser gas is also subjected to erosion and shock heating, but strong cooling can overall slow down these

processes. As a result, not all the gas is heated up to temperatures  $T \gtrsim 10^6$  K by the end of the simulation time.

Figure 4 shows the time evolution of the mass-weighted 2D phase diagrams of temperature versus number density of cloud material for our control adiabatic and radiative models with  $\delta = 16$ . In the adiabatic model, the cloud material experiences rapid heating, with the majority of the material reaching temperatures  $T > 10^4$  K in only  $t_{\text{sim}} = 0.6$  Myr. Due to the absence of mechanisms to release the extra energy injected via shocks, the cold gas is heated up, thus leaving little dense material at low temperatures. By  $t_{\text{sim}} = 2.1$  Myr, most of the cloud mass corresponds to hot gas with temperatures  $T \gtrsim 10^5$  K which has also expanded transversely (i.e. along the X and Z directions, see Figure 2). The radiative model exhibits a different thermodynamic evolution. In the early stages of the simulation ( $t_{\text{sim}} = 0.6$  Myr), the cloud gas pushed downstream by the wind is initially heated up, but then gradually cools down to temperatures  $T \sim 10^4$  K. Cooling also leads to geometrically thinner tails of cloud material (see Figure 2). During most of the simulation time, two distinct gas phases are observed: a cooler and denser phase with  $T \sim 10^4$  K and  $n \sim 1 \text{ cm}^{-3}$ , and a higher-temperature and lower-density phase with  $T \sim 10^6$  K and  $n \sim 0.01 \text{ cm}^{-3}$ . The overall flow is therefore multi-phase, and resembles the observed structure of galactic winds.

### 3.1.2 Gas Mixing and cloud dynamics

Figure 3 also depicts the mixing fraction between wind and cloud gas (equation 7), the cold gas mass fraction (equation 9), and the mass-weighted average velocity in cloud material (equation 5) for our control adiabatic and radiative  $\delta = 16$  models. Both models exhibit a high degree of turbulence and mixing. In the adiabatic model, turbulent mixing and dispersion processes are associated with the generation of vortical motions via KH instabilities during the whole evolution and via RT instabilities at the late stages of the interaction (also seen in adiabatic wind-cloud simulations, e.g. Banda-Barragán et al. 2016; Pittard & Parkin 2016). Shear instabilities lead to mixing, erosion of low-density regions in the clouds, and the formation of geometrically thick tails downstream of each cloud.

On the other hand, in the radiative model, mixing and dispersion arise not only from KH and RT instabilities, but also from cooling-induced pressure gradients and turbulence driven by condensation (see Ji et al. 2019; Fielding et al. 2020 for further details on radiative mixing layers). As a result, radiative models exhibit a higher degree of mixing compared to adiabatic models (see Figure 3). Condensation occurs from the early stages of evolution of radiative models, where warm mixed gas with  $T \sim 10^{4.5} - 10^{5.5}$  K efficiently condenses into colder and denser material as the cooling rates peak at those temperatures. Condensation thus promotes the formation of a denser medium and geometrically thin tails behind the clouds (see Figure 2). Gas along such tails fragments into smaller gas clumps as time progresses, which results in the emergence of a narrow stream of dense and turbulent clumpy gas.

Radiative mixing also influences the cold gas mass fraction and the dynamics of cloud gas. Panel (e) of Figure 3 shows that the radiative model preserves cold material (with  $T < 10 T_{\text{cl}}$  for a significantly longer period compared to the adiabatic model. This occurs as a result of: 1) the delayed growth of KH instabilities thanks to the larger density contrasts caused by cooling-driven contraction, and 2) re-condensation of shocked cloud material that has already mixed and dispersed downstream of each cloud. On the other hand, Panel (f) of Figure 3 shows that the cloud velocities in the adiabatic model are higher compared to the radiative one. Radiative models are subjected to efficient cooling of the warm, mixed gas, which leads to the

formation of higher column densities. Denser gas occupies a smaller volume, so it is more difficult to accelerate via direct momentum transfer (see Scannapieco & Brüggen 2015; Banda-Barragán et al. 2016). Conversely, the expansion of adiabatic clouds results in larger cross sections and a higher rate of cloud acceleration. Towards the end of the simulations, however, we see that radiative clouds reduce the gap as gas that condenses back into the cold phase preserves some of the momentum that was present in the warm phase (see discussion in Schneider et al. 2020; Banda-Barragán et al. 2021).

## 3.2 Hydrodynamic shielding

The arrangement of clouds in a stream-like formation affects how they interact with the surrounding wind compared to isolated cloud formations. While isolated clouds are subjected to strong drag forces (Banda-Barragán et al. 2019), clouds along gas streams have the capacity to hydrodynamically shield one another from disruption (caused by their interaction with the wind gas, see Alūzas et al. 2012; Banda-Barragán et al. 2020). As noted in the previous section, the morphology of downstream clouds is not only influenced by the background wind, but also by the upstream clouds. Two processes are crucial for hydrodynamic shielding in multi-cloud systems: the first one involves the reduction of drag forces on individual clouds (which lessens acceleration and delays RT instabilities), and the second one is the interaction between clouds as a result of the displacement induced by the supersonic wind (which eventually leads to collisions between upstream cloud tails and downstream cloud cores). Generally, then, cloud material subjected to hydrodynamic shielding can persist for longer periods due to its ability to survive dynamic shredding and drag.

The filaments created from the stripping of the outer layers of the clouds, as a result of instabilities, serve as a protective cover for the downstream cloud cores once they reach them. As the wind continues to flow downstream, it also interacts with downward clouds which means that part of the gas that already directly interacted with the preceding cloud, starts to interact with downstream clouds. This means that the evolution of the individual clouds along the gas stream is not independent, but relies on their interaction with: 1) the hot wind, 2) the other clouds further upstream, and 3) mixed gas that has already interacted with upstream cold material. The higher the separation distance ( $\delta$ ) within the clouds, the less probable it is for hydrodynamic shielding to act; and vice versa. This means there is a threshold value for the separation distance,  $\delta_{\text{shield}}$ , so that when  $\delta < \delta_{\text{shield}}$ , hydrodynamic shielding occurs. As we discuss below, the value of  $\delta_{\text{shield}}$  varies between subsonic and supersonic cases and between adiabatic and radiative simulations.

### 3.2.1 The role of the inter-cloud separation distance ( $\delta$ )

Figure 5 and 6 show 2D slices at  $Z = 0$  of the gas number density for several separation distances, ranging from  $\delta = 2$  to  $\delta = 64$ , for adiabatic and radiative models, respectively. The effects of placing a group of cold clouds in a hot background wind vary widely with  $\delta$ . Clouds, separated by large distances (i.e. with high  $\delta$  values), are unable to withstand the hydrodynamic drag forces, and disintegrate and mix with the surrounding medium at a very fast pace. In contrast, groups of clouds, separated by systematically smaller distances are able to reduce drag and preserve increasingly larger fractions of dense gas. Thus, reducing the separation distance between clouds results in a substantial increase in hydrodynamic shielding. When the separation value is set to  $\delta = 64$ , the cloud can be considered as

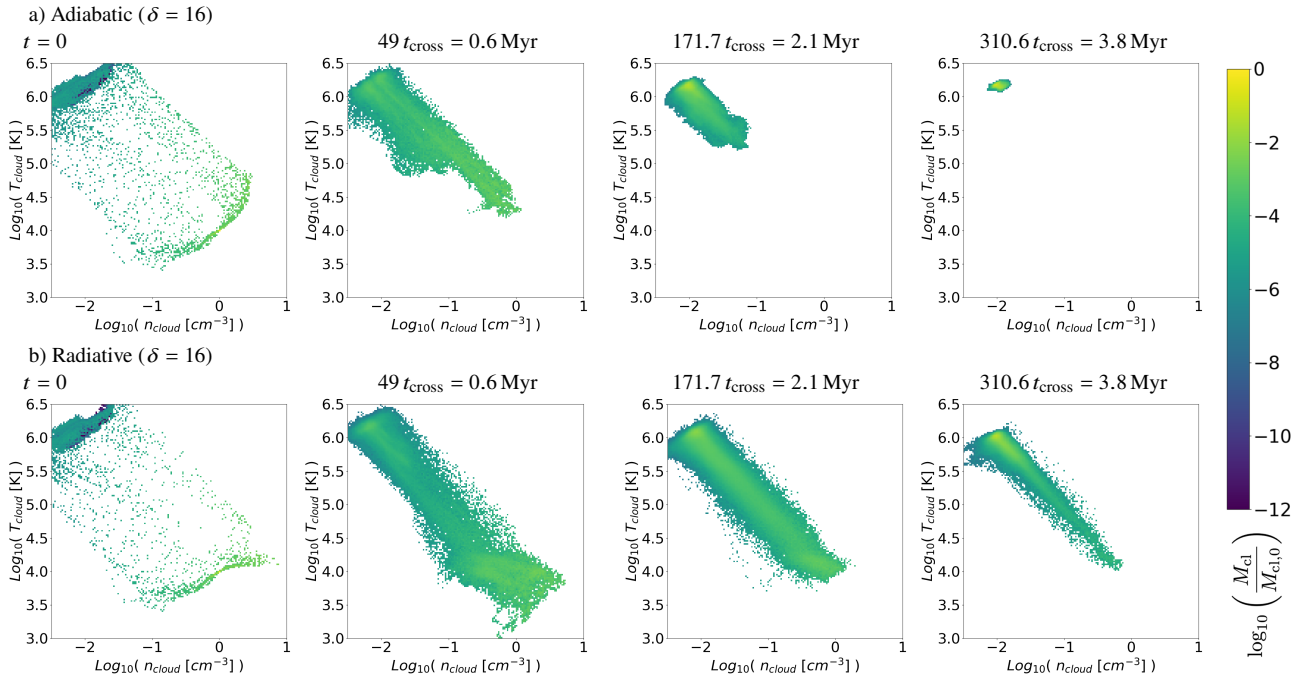


**Figure 4.** Mass-weighted phase diagrams displaying the two-dimensional distributions of temperature and density of cloud material in the adiabatic (top) and radiative (bottom)  $\delta = 16$  model at five different times through the simulation (columns). Without mechanisms to release the excess energy injected by shocks, the cold gas in adiabatic clouds heats up and becomes unstable, leading to a shortage of dense cloud material at low temperatures. The radiative model exhibits a slower heating rate than the adiabatic case, resulting in a multiphase structure with a cooler, denser phase and a less dense, hotter phase.

quasi-isolated because hydrodynamic shielding is absent. Therefore, there is a significant difference between quasi-isolated clouds that are rapidly disrupted and those that provide mutual shielding.

Closely-spaced clouds can effectively act as a cylindrical-like stream of cold material, and whether hydrodynamic shielding occurs or not depends on how fast information from upstream clouds travels downstream. Following (Forbes & Lin 2019), we define the shielding time-scale ( $t_{\text{shield}}$ ) within which an upstream cloud can influence a downstream cloud, altering its morphology and physical properties, as the time it takes for information from the upstream cloud to reach the downstream cloud. In subsonic cases,  $t_{\text{shield}}^{(\text{sub})} \approx t_{\text{cc}} + t_{\text{sc}} = \delta_{\text{shield}} r_{\text{cl}} / c_{\text{wind}}$ , which results in a threshold separation distance of

$$\delta_{\text{shield}}^{(\text{sub})} \approx \sqrt{\chi} \left( 1 + \frac{1}{M_{\text{wind}}} \right) \quad (11)$$

In supersonic cases (like our models), the flow exceeds the wind sound speed, so  $t_{\text{shield}}^{(\text{sup})} \approx t_{\text{cc}} = \delta_{\text{shield}} r_{\text{cl}} / c_{\text{wind}}$ , which results in a much smaller threshold separation distance of

$$\delta_{\text{shield}}^{(\text{sup})} \approx \sqrt{\chi} \left( \frac{1}{M_{\text{wind}}} \right) \quad (12)$$

### 3.2.2 Hydrodynamic shielding in subsonic vs. supersonic cases

In Figure 7, we report the evolution of various parameters, such as the mass-weighted average temperature, the mean density, and the dense gas mass fraction of cloud material, for both adiabatic and radiative models. All the curves follow the same trends discussed in Section 3.1, i.e. cloud gas in adiabatic models reaches higher temperatures,

loses more mass, and retains less dense gas than their radiative counterparts. In addition, we see more effects: (i) a very clear dependence on  $\delta$  as the trend indicates that the closer the clouds are placed, the best the protection against shredding and erosion of cold material, which in turn prevents a drastic increase in temperature, (ii) the threshold separation distance for hydrodynamic shielding to occur is smaller in our supersonic models than in the subsonic and transonic models reported in (Forbes & Lin 2019), and (iii) hydrodynamic shielding operates differently in adiabatic and radiative models.

Regarding point (ii), we find that for adiabatic models the threshold separation distance of supersonic cases becomes much smaller than in subsonic cases (cf. Figure 2 in Forbes & Lin 2019, where a smoother transition can be seen for increasing  $\delta$  values). For our wind Mach number, using equation 12 we obtain  $\delta_{\text{shield}}^{(\text{sup})} \sim 3$ , which is in agreement with the results presented in Figures 7, particularly with  $f_{\text{dense}}$  (top right panel in Figure 7). This panel shows strong hydrodynamic shielding only for  $\delta \lesssim 4$  (much smaller than what the subsonic equation 11 predicts), and very weak or no shielding for larger distances. It is clear that hydrodynamic shielding in adiabatic supersonic cases requires very small separation distances between the clouds, which is reasonable considering that clouds can be disrupted faster than what hydrodynamic shielding requires to develop.

### 3.2.3 Hydrodynamic shielding in adiabatic vs. radiative models

Regarding point (iii), we find that smaller  $\delta$  values have a higher impact on radiative clouds than they do on adiabatic clouds, pointing to differences in how hydrodynamic shielding operates in adiabatic and radiative models. In radiative cases, cooling promotes the precipitation of warm material into the cold phase, contributing to the preservation of gas with temperatures  $T < 10^5$  K. Re-condensed gas arising from mixed layers then offers protection to downstream

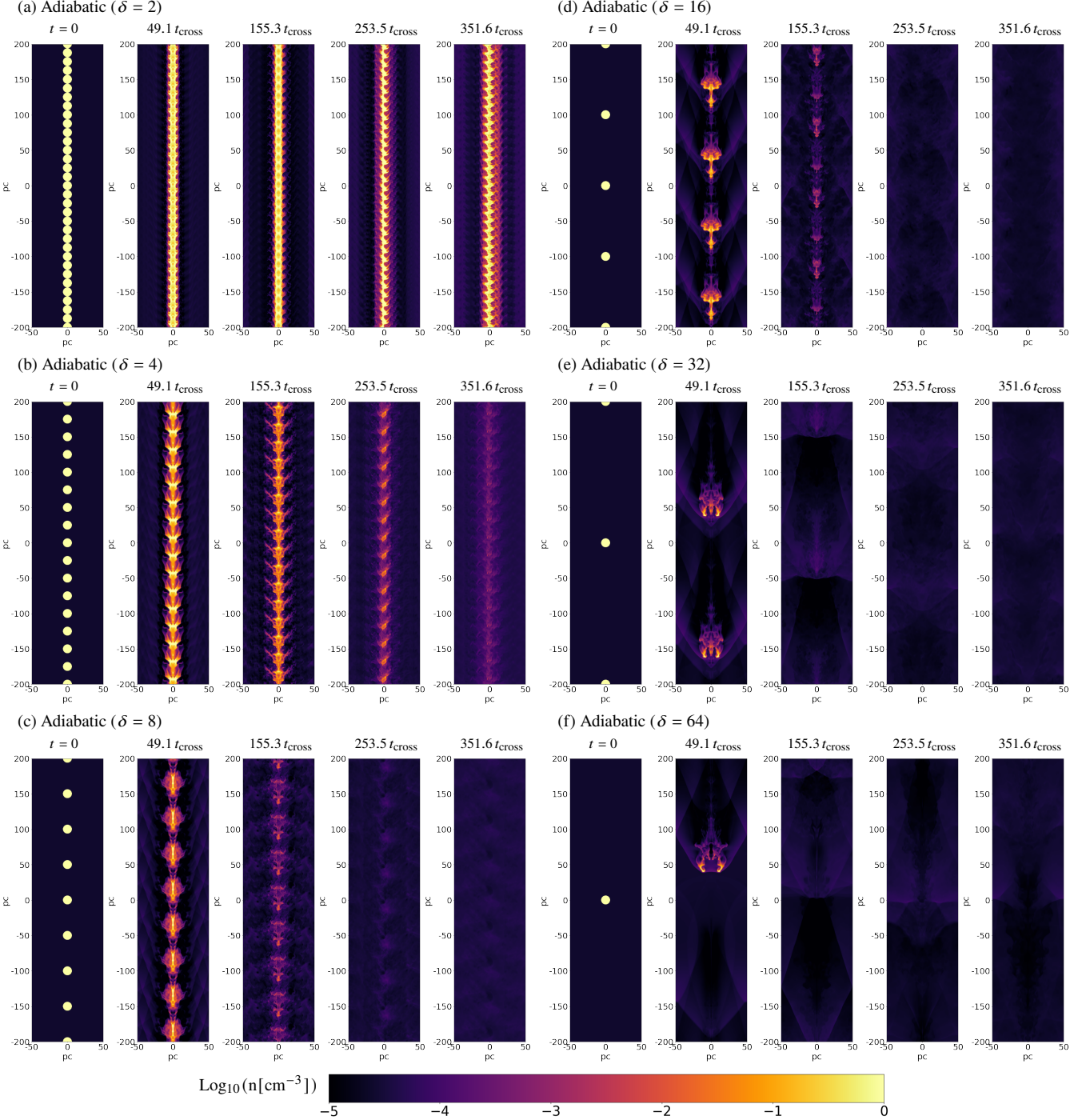


**Figure 5.** 2D slices at  $Z = 0$  of the gas number density in adiabatic models with different cloud separation distances of  $\delta = 2$  (upper left panel),  $\delta = 4$  (middle left panel),  $\delta = 8$  (lower left panel),  $\delta = 16$  (upper right panel),  $\delta = 32$  (middle right panel), and  $\delta = 64$  (lower right panel) at five different times through the simulation (shown in columns). Hydrodynamic drag forces cause clouds separated by large distances to disintegrate and mix completely with the surrounding medium at a rapid pace. In contrast, a group of closely spaced clouds have the capacity to shield each other from drag forces and the erosive effects of dynamical instabilities.

dense cloud cores by reducing drag forces. Additionally, dynamical instabilities are not as effective in the radiative cases owing to the higher densities, so dense material is preserved in stream-like structures. Compared to adiabatic models, we find that radiative models consistently exhibit a longer lifespan of dense cloud material for all  $\delta$  values. This is due to the combination of radiative cooling and

hydrodynamic shielding. As an example, when the separation value is  $\delta = 2$ , the arrangement preserves a dense gas mass fraction of  $\sim 30\%$  in the adiabatic run and  $> 70\%$  in the radiative run by the end of the simulation period ( $t \sim 5$  Myr).

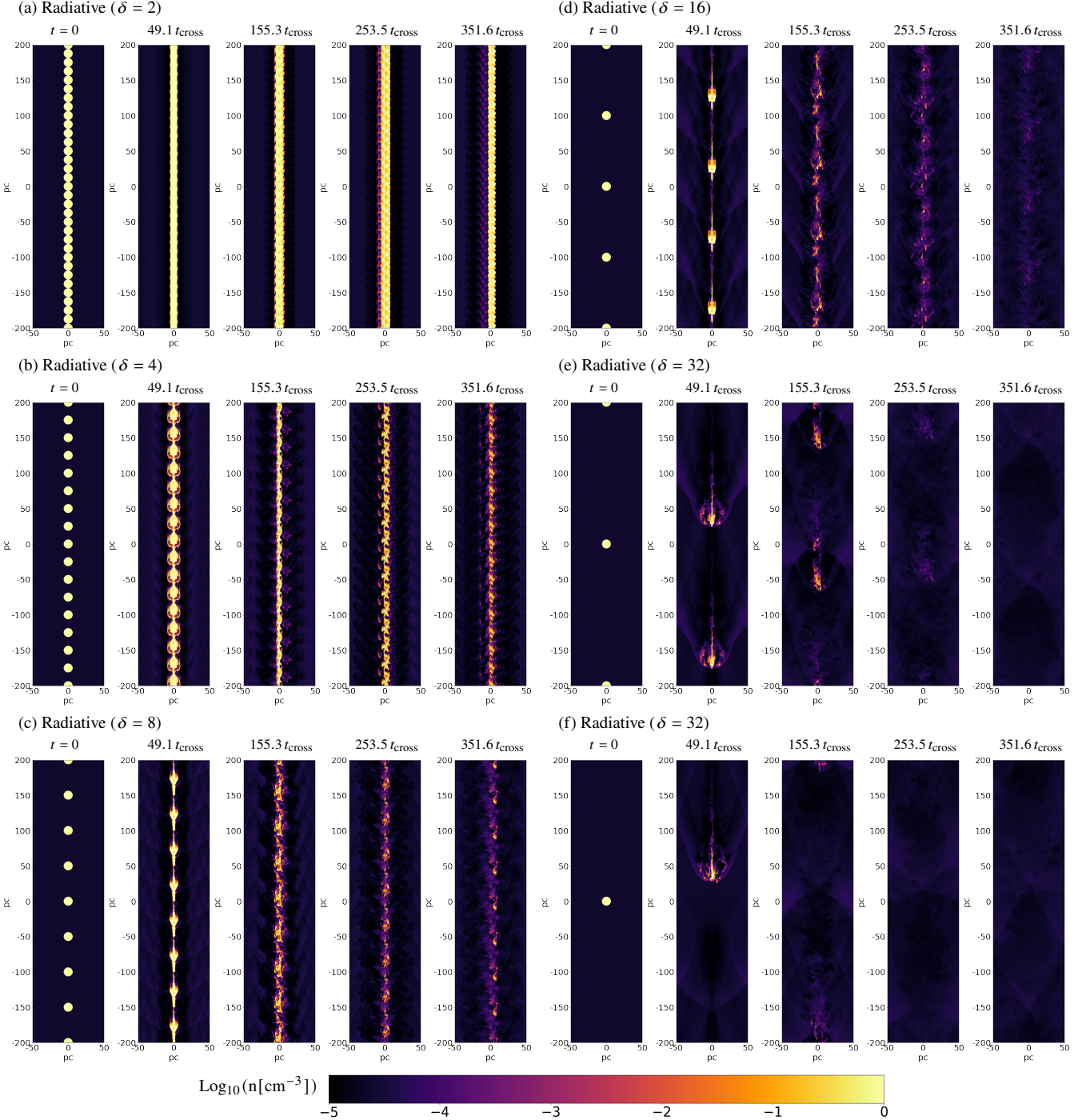


**Figure 6.** 2D slices at  $Z = 0$  of the gas number density in radiative models with different cloud separation distances  $\delta$  (top left panel),  $\delta = 4$  (middle left panel),  $\delta = 8$  (bottom left panel),  $\delta = 16$  (top right panel),  $\delta = 32$  (middle right panel), and  $\delta = 64$  (bottom right panel) at five different times through the simulation (columns). Cooling can form a multiphase medium characterised by continuous condensation, which allows for the preservation of a large fraction of dense gas. Interactions between clouds shield the cold material in downstream clouds from drag forces from the background medium by interposing a layer of disrupted warm material. This reduces the effective drag forces acting on downstream clouds. Decreasing the inter-cloud separation distance results in a much smoother transition. This is because the hydrodynamic shielding effect is more pronounced when we consider radiative cooling at smaller separation distances, which helps to mitigate the disruptive effects of the drag force.

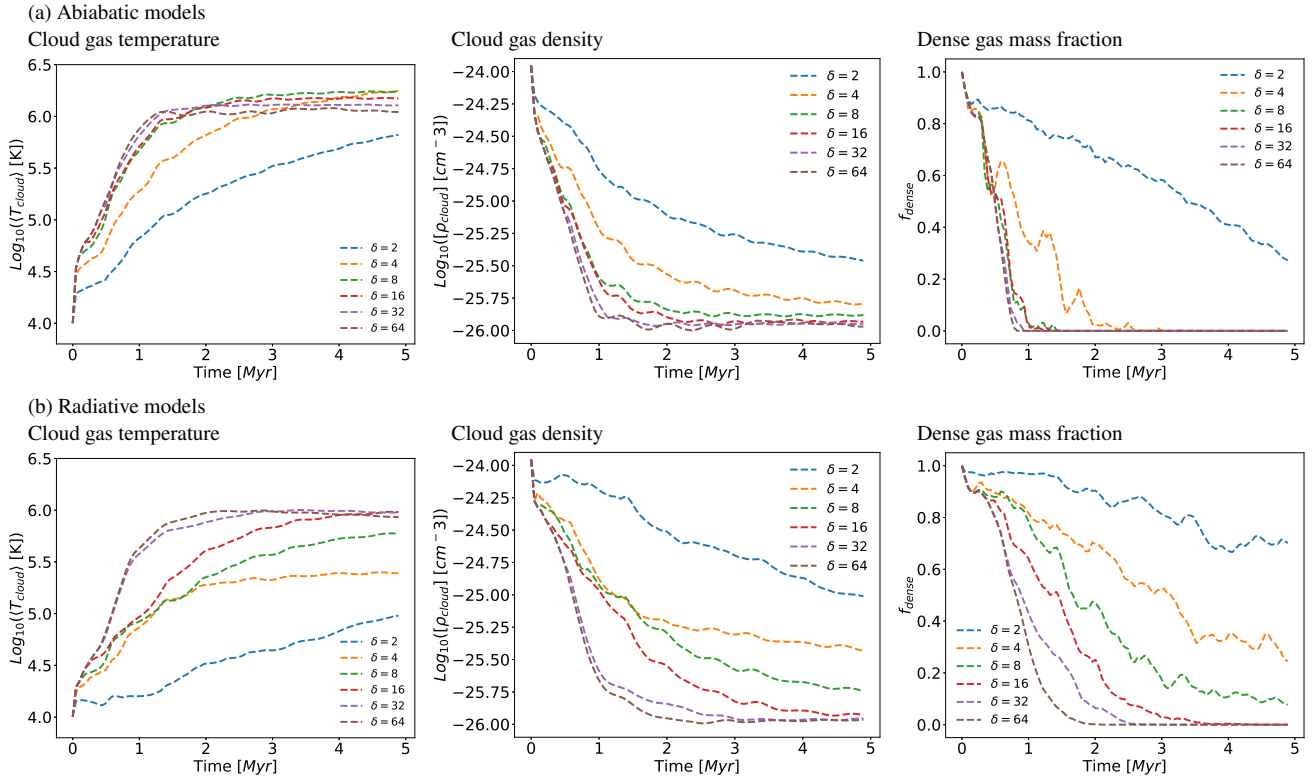


**Figure 7.** Time evolution of the mass-weighted average temperature (left column), mean density (middle column), and dense gas mass fraction (right column) for different values of the parameter  $\delta$  in the adiabatic (top) and radiative (bottom) models. Closer cloud spacing enhances the protection of cold material from shredding and erosion, preventing a drastic temperature increase. Smaller  $\delta$  values significantly impact clouds by shielding dense cores from upstream clouds with mixed layers of intermediate-density material, promoting the precipitation of warm material into the cold phase and contributing to gas preservation.

### 3.2.4 Cloud mixing and survival of cold gas

The left-hand side column of Figure 8 shows the mixing fractions in both adiabatic and radiative models. We find that: (i) all models exhibit significant differences as we change the value of  $\delta$ , but, (ii) for a fixed  $\delta$ , mixing fractions in adiabatic cases are always lower than in their radiative counterparts. Regarding (i), the models with larger  $\delta = 16, 32, 64$  show similar mixing profiles, indicating that when clouds are further apart, there is greater disruption by KH and RT instabilities. In contrast, when clouds are closer together, i.e.  $\delta = 2, 4, 8$ , the degree of mixing is reduced due to hydrodynamic shielding, which protects the clouds from instabilities. Regarding (ii), unlike adiabatic clouds, radiative clouds undergo mixing due to instabilities as well as turbulence and cooling-induced pressure gradients driven by condensation. As a result, mixing is not as fast and efficient in adiabatic models as in radiative models. This is in agreement with the results presented in Banda-Barragán et al. (2021) (cf. with their Figure 7).

Mixing also has a direct influence on the cold gas content. The middle column of Figure 8 shows the same effects as before with clouds in closer configurations retaining more cold material than clouds with large  $\delta$ , and radiative clouds showing higher amounts of cold gas compared to their adiabatic peers. For instance, in the  $\delta = 2$  case, the adiabatic model retains 40% of its cold gas material by the end of the simulation time ( $\sim 5$  Myr), while higher  $\delta$  models lose all their cold gas and the radiative model is able to retain more than twice this amount, holding over  $\sim 90\%$  of the initial cold cloud material. Thus, hydrodynamic shielding and the condensation mechanism prove to be particularly powerful in this regard, helping to

maintain cold gas throughout the entire simulation period. Radiative models trigger re-condensation of mixed gas, which also allows for a smoother transition in cold gas content among simulations with different  $\delta$  values, compared to adiabatic models where a very sharp transition occurs for  $\sim \delta_{\text{shield}}^{(\text{sup})}$ .

### 3.2.5 Cloud gas dynamics

The right-hand column of Figure 8 shows that the mass-weighted velocity of the clouds also increases as the separation distance  $\delta$  increases. In other words, clouds that are spaced closer together will take longer to reach a higher velocity. This can be attributed to the fact that a smaller  $\delta$  value results in the formation of larger column densities. Gas with larger column densities is harder to accelerate via direct momentum transfer from the wind as it has more inertia. We also observe that the adiabatic model has a higher velocity compared to the radiative model. This observation has important implications for the cold gas entrainment, which is the process by which material from the ISM/CGM becomes mixed and carried along by the outflowing galactic wind (Veilleux, Rupke & Swaters 2009). Entrainment of dense gas then depends on the interplay between hydrodynamic shielding and radiative processes. Specifically, our results suggest that the efficiency of radiative cooling reduces the strength of the hydrodynamic drag forces acting on the clouds and therefore impact the entrainment velocity of dense gas. The subsonic and transonic wind-micloud simulations presented by (Forbes & Lin 2019) showed a very similar trend (cf. our results with their Figure 3).

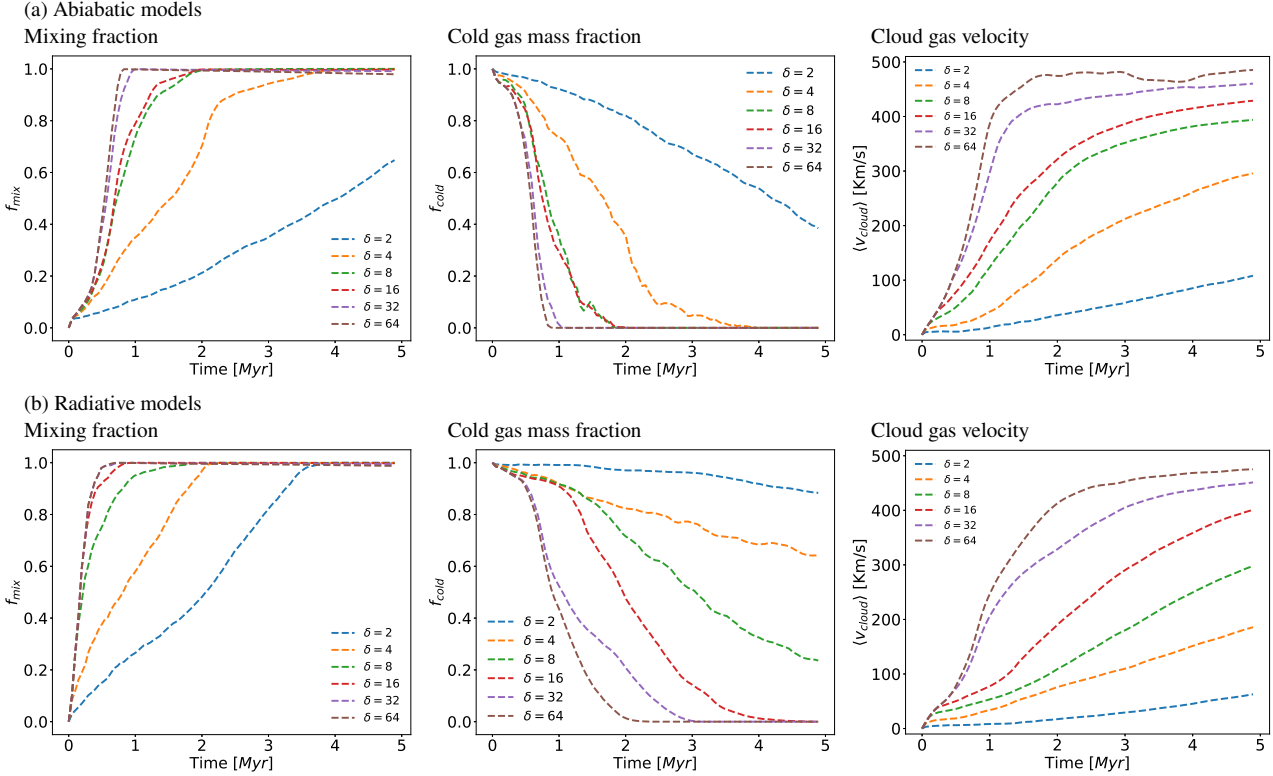


**Figure 8.** Time evolution of the mixing fraction (left column), cold gas mass fraction (middle column), and mass-weighted average velocity (right column) for different values of the parameter  $\delta$  in the adiabatic (top) and radiative (bottom) models. Hydrodynamic shielding reduces mixing and enhances condensation in both models when clouds are closer together. This is because hydrodynamic shielding protects the clouds from instabilities, while reduced drag forces promote condensation. As a result, the cold gas is maintained throughout the simulation. As tighter arrangements trigger the generation of large column densities, the velocity of cloud material decreases with decreasing separation distance  $\delta$ .

### 3.3 Implications

In this section, we discuss the implications of our study for the physics of galactic winds and compare our findings with previous studies. [Forbes & Lin \(2019\)](#) conducted a similar set of simulations to ours, focusing mainly on the velocity and the cold gas mass fraction. Their simulations were scale-free and only focused on the hydrodynamics of the gas, which means that the results can be applied if the density contrast and Mach number are similar to what they used. Our simulations, on the other hand, include physical units, time scales, and radiative processes. We also considered a wind with  $M_{wind} = 3.5$ , consistent with the CC85 model, while [Forbes & Lin](#) used both,  $M_{wind} = 0.31$  and  $M_{wind} = 1$ , which produced some differences in the behaviour of mass conservation and acceleration. Despite the different initial conditions, both studies are consistent in showing that adiabatic clouds approach the background wind velocity and have the potential to retain more cold gas mass as the clouds are arranged in closer configurations at  $t = 0$ . The implementation of a supersonic hot background in our simulations introduces some differences from the previous work. As observed in the previous study, increasing the  $M$  of the wind reduces the cold gas mass that is retained, while reducing it makes the cloud take more time to accelerate. Additionally, our study reveals that increasing the velocity of the background to supersonic velocities not only decreases the amount the cold gas mass retained by the system but also leads to a longer time for the cloud material to reach the high background velocity. This outcome was expected, particularly in the radiative case, where the increase in

the velocity of the clouds highly depends on the formation of density columns.

It is necessary to compare our study to other numerical studies that address similar questions in parts of the ISM. For instance, [Aluzas et al. \(2012\)](#) investigated the interaction between a shock and regions containing multiple individual clouds randomly distributed. Their findings indicate that downstream clouds are affected by their interaction with the shock, which results in a lower cloud lifetime compared to clouds located on upstream blocks of the simulation domain. The behaviour of the clouds observed in that study is consistent with the findings presented in our study. While Aluzas randomly distributes groups of clouds in the simulation domain, it is possible that some of that clouds are positioned downstream of each other. As we have demonstrated in this work, that kind of arrangement triggers hydrodynamic shielding, which leads to dense shells of gas due to the protection that upstream clouds provide to downstream clouds.

Another relevant study is the one conducted by [Banda-Barragán et al. \(2020\)](#). They reported three-dimensional hydrodynamical simulations of a shock interacting with multicloud layers, considering solenoidal and compressive cloud layers, with the inclusion of radiative heating and cooling. Their results show that the dynamics and disruption of a multicloud system depend on the number of cloudlets in the layer. They found that for a more compact system with a high number of cloudlets, turbulence, and mixing are reduced, which is in agreement with our results. This is in agreement with our results, as we previously established that if the distance between clouds is decreased, hydrodynamic shielding reduces the effect of dynamical

instabilities, which results in a lower mixing fraction. Furthermore, their findings revealed that simulations considering radiative cooling showed that the cooling of mixed gas may explain the presence of dense gas observed in galactic outflows. Our results are consistent with this statement, as we have shown that when we consider radiative processes, dense gas can be maintained for several Myrs by acquiring large column densities. These large column densities are also generated when we have a system with a large number of cloudlets i.e. clouds that are very close to each other. In the compact models presented in that study, the bulk speed is lower than in solenoidal models, as in our simulations where the models with clouds closer to each other diminish the acceleration due to the presence of large column densities. Moreover, the authors of those studies indicated that when we consider radiative cooling, cold material acquires momentum from mixed cloud gas, which is in line with the behaviour of our clouds, where there is not a direct momentum transfer, but momentum is transmitted from the warm phase when this material is condensed to the cold phase.

Let us now direct our attention to research studies that focus on global galaxy simulations. The work carried out by Schneider et al. (2018, 2020) presented a set of high-resolution simulations of isolated galaxy models. Their study indicated that mixing and radiative cooling work as sources of fast-moving cool gas, which can be observed in absorption-line studies of outflows around star-forming galaxies. Our work, on the other hand, focuses on patches of the CGM, and it highlights that radiative gas expelled from supernova feedback can be accelerated to velocities of several hundred kilometres per second before being destroyed (due to radiative cooling and hydrodynamic shielding). We previously established that mixing between hot and cold gas provides an effective way of transferring momentum from one phase to another. In agreement with Schneider et al. (2020), our models show that gas mixing is deeply connected to dense gas entrainment (i.e. mixing facilitates momentum transfer). This results in a proportional relationship between the mixing fraction and the velocity of the cloud material, thus being consistent with the work of Schneider et al.

An important aspect to highlight is that our work is complementary to those previous studies mentioned above, as our models cover a different parameter space, show that hydrodynamic shielding also occurs in radiative scenarios, and provide support to results reported from larger-scale models where the numerical resolution is not sufficient to capture hydrodynamic shielding and separate it from other effects.

#### 4 NUMERICAL RESOLUTION AND LIMITATIONS

In this section, we discuss how the numerical resolution of our simulations influences the numerical results that we report in this paper. We carried out a total of 8 additional simulations for both adiabatic and radiative models. Figure x shows the time evolution of the previous numerical analysis of the adiabatic and radiative model respectively using the standard separation values  $\delta = 8, 16$  for the low- $(R_8)$ , standard- $(R_{16})$ , and high- $(R_{32})$  resolution simulations.

In the adiabatic model, all the quantities tend to converge, regardless of the separation value being analyzed. However, the thermodynamic path followed by the quantities is not identical, although they do reach similar convergence values across all models. Additionally, the time at which the convergence value is reached is also similar across all the models. In contrast, when radiative processes are considered, there is a spread in the trends observed. The first and third rows show the mass-weighted average temperature, the mean

density, and the dense gas mass fraction in cloud material for both models. We observe that for  $\delta = 16$ , both high and standard resolutions show a similar temperature trend, which suggests convergence. However, when it comes to  $\delta = 8$ , the temperature path varies significantly across all resolutions, and convergence is not achieved. We attribute this to the differences in the mixing profiles in these models, which depend on small-scale phenomena (e.g. turbulence in radiative layers), which do not necessarily converge. Generally, the mean density and the dense gas mass fractions diverge as  $\delta$  decreases, as cloud-cloud interactions occur more frequently, leading to more condensation and precipitation mechanisms that alter the gas structure. Therefore, for small  $\delta$  values, the numerical quantities are expected to be somewhat divergent. In contrast, for large separation values, the standard and high-resolution models exhibit similar behaviour after half the simulation time, leading to convergence for both models.

The second and fourth rows show the mixing fraction, the cold gas mass fraction, and the mass-weighted velocity of cloud material for both models. In the radiative model, all resolutions can capture the cooling-induced pressure gradients for both large and small  $\delta$  values. In general, variables that depend on the generation of turbulence exhibit some deviations when resolution is increased for both models, but ultimately, the trends agree and show convergence. The cold gas mass fraction is closely linked to the average temperature of the cloud material. As seen previously for large separation values  $\delta$  standard and high-resolution simulations converge with slight deviations. However, for small separation values, there are important deviations in the paths followed by each simulation. Since the temperature does not converge, the cold gas mass fraction exhibits similar behaviour with all the simulations having different paths and values at the end of the simulation time. In general, for thermodynamic quantities and small  $\delta$  values, numerical quantities tend to be more divergent as they depend on smaller-scale effects. On the other hand, the behaviour of the cloud velocity remains consistent regardless of the chosen resolution. As previously discussed, the acceleration of radiative clouds is not due to direct momentum transfer but rather momentum conservation from warm material. Based on the evolution of these specific variables, we can conclude that all resolutions correctly capture the dynamics of the multi-cloud system for the adiabatic and radiative systems.

While the analysis of hydrodynamic interactions between two gas phases (cold clouds and hot winds) provides an overall view of the galactic outflows, it is essential to acknowledge the limitations of our numerical work due to the exclusion of additional physics in our study. Self-gravity is one such aspect, not included in our models, that may affect the evolution of clouds. Our radiative clouds undergo compression, so some regions of them could become marginally gravitationally unstable had self-gravity been included. This phenomenon has been observed in our specific context of cold, dense spherical clouds moving through a hot medium (see Murray et al. 1993). In other scenarios, it has been proved that the inclusion of electron thermal conduction has a significant impact on the way clouds interact with the wind, leading to changes in their morphology, mass loss rate, and velocity (see Brüggen & Scannapieco 2016). The acceleration of cold clouds by the ambient background is hindered by thermal conduction, which can alter the dynamics of the system in various ways. In addition, it is important to note that this study did not incorporate magnetic fields. Magnetohydrodynamic (MHD) scenarios are known to significantly affect the dynamics and survival of dense gas (see Banda-Barragán et al. 2018). Therefore, it is crucial that future studies conduct MHD simulations of wind-microlens systems that incorporate self-gravity and electron thermal

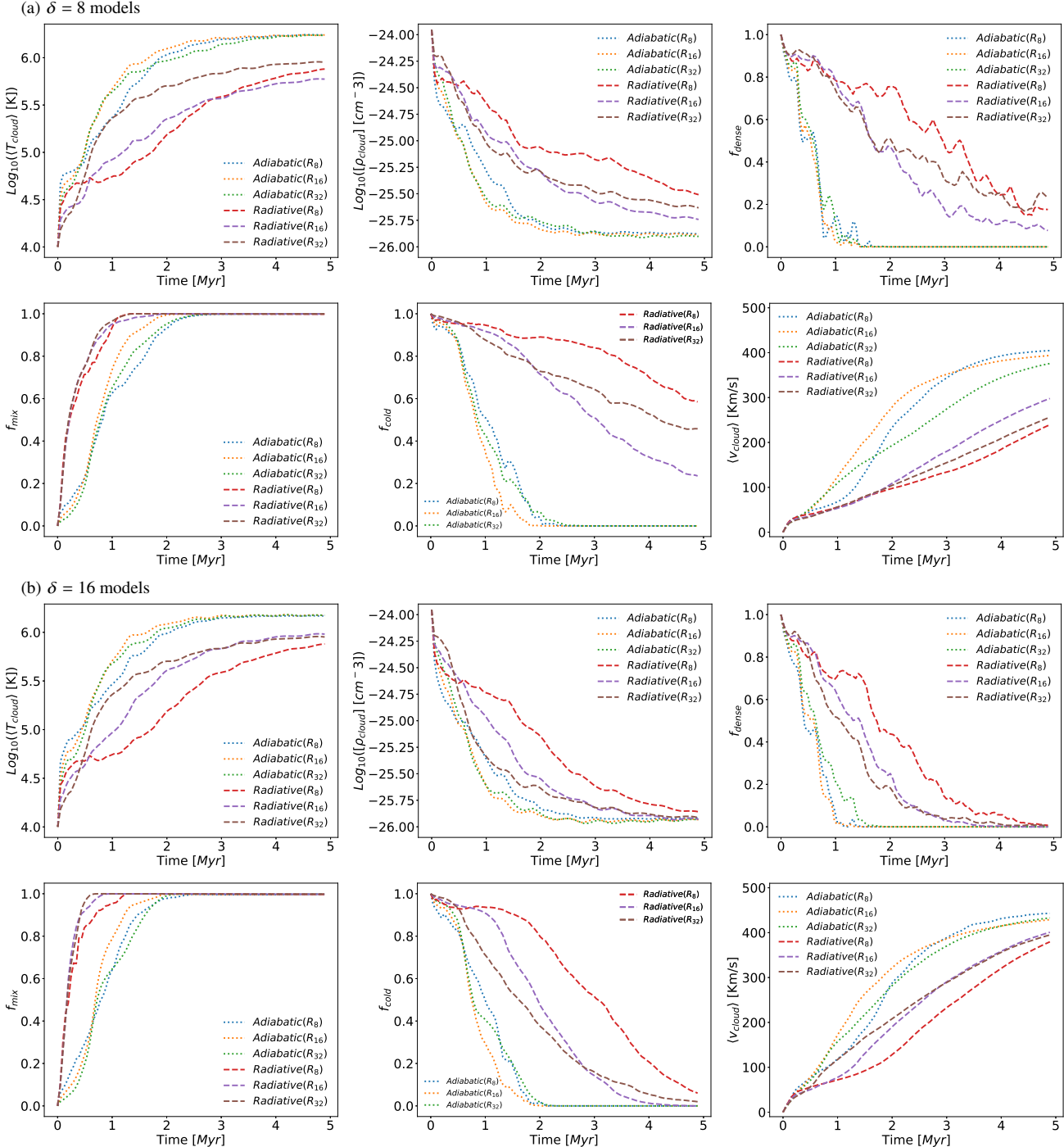


**Figure 9.** Convergence Analysis of the time evolution for various numerical analyses of the adiabatic and radiative models for  $\delta = 8$  (top two rows) and  $\delta = 16$  (last two rows). Adiabatic models exhibit overall convergence in all quantities, regardless of separation distance. When radiative processes are considered for small separation values, turbulence-dependent variables initially exhibit slight deviations between standard and high resolution, but ultimately converge with time. Physical quantities affected by the condensation mechanism diverge as the separation distance decreases due to the increased frequency of cloud-cloud interactions.

conduction to further investigate the magnetic field effects on cloud dynamics and hydrodynamic shielding.

## 5 CONCLUSIONS

The aim of this paper was to evaluate the efficiency of hydrodynamic shielding and radiative cooling in preserving dense cold gas by means of numerical models of systems of multiple clouds with  $T \sim 10^4$  K and embedded in a hot supersonic ambient wind with  $T \sim 10^6$  K and

$M = 3.5$ . This research was carried out by analysing the behaviour of multicloud systems with different separation distances ( $\delta$ ) between the clouds. The main findings of this thesis are summarised below:

- The overall evolution of wind-multicloud models can be divided into four distinct stages: i) The wind material collides with the front surface of the upstream clouds, producing both reflected and refracted shocks; ii) Clouds begin to lose mass through stripping caused by KH instabilities from their surface layers; iii) The upstream motion of the wind leads to the collision between the filamentary tails of upstream clouds with the cores of downstream clouds; iv) Clouds have undergone a substantial mass loss, and their acceleration has reached a level that triggers the growth of RT instabilities. These instabilities ultimately cause the destruction of clouds, as low-density bubbles penetrate dense layers of remaining cloud material (see Section 3.1).
- Our models of adiabatic clouds, which lack an efficient energy release mechanism, are eventually heated and shredded. In contrast, the radiative models show that efficient cooling can remove energy that would otherwise be converted into heat. This, combined with cooling-induced pressure gradients, promotes condensation and mixing, which aid the survival and re-formation of dense clouds as the cold gas is shielded from instabilities. Adiabatic clouds are rapidly destroyed due to the presence of KH instabilities, which make it impossible for them to retain cold gas. Conversely, radiative clouds exhibit a multiphase structure characterized by both a cooler, denser gas phase, and a lower-density, higher-temperature gas phase. In adiabatic models, mixing occurs due to KH and RT instabilities, while radiative clouds experience additional mixing due to cooling-induced pressure gradients. Adiabatic clouds obtain their acceleration through direct momentum transfer, whereas radiative clouds retain some of the momentum present in the warm phase as they condense back into the cold phase thanks to efficient cooling (see Section 3.1.1).
- Dynamic and thermodynamic differences arise when we change the initial separation distance between the clouds,  $\delta$ . The morphology of downstream clouds is not only influenced by the wind but also by the tails of upstream clouds that eventually collide with them. When the separation value is decreased, our models show that there is a significant increase in hydrodynamic shielding, as the effective drag force acting on individual downstream clouds is reduced. This leads to the preservation of dense material for a longer period of time. Closely-spaced arrangements have a substantial impact on the clouds, as they offer protection to the dense cloud cores from the mixed turbulent layers of intermediate-density material produced by upstream clouds. This material is preserved in stream-like structures, reducing the growth rate of instabilities while also facilitating the condensation of cold material (see Section 3.2.1 and 3.2.2).
- The degree of mixing between clouds is linked to their separation distance. The further apart the clouds are, the greater the chance of generating dynamic instabilities, which enhances the degree of mixing. When clouds are closer to each other, the condensation mechanism is particularly powerful as the effective drag forces are drastically reduced, helping to maintain the cold gas throughout the entire simulation period. The mass-weighted velocity of cloud material decreases as the separation value  $\delta$  decreases, as tighter arrangements trigger the generation of large column densities (see Section 3.2.3 and 3.2.4).
- When examining adiabatic models, we found that regardless of the separation distance being considered, there is overall convergence in all the quantities. When radiative processes are taken into account, the standard-resolution and high-resolution models display a similar behaviour for large separation values, particularly after half the simulation time, leading to convergence. However, when it comes

to small separation values, variables that depend on turbulence generation initially exhibit slight deviations between standard and high resolution, but as we move forward in time, they ultimately converge. The physical quantities that are affected by condensation and precipitation mechanism exhibit divergence as  $\delta$  decreases, as cloud-cloud interaction occurs more frequently (see Section 4).

Overall, our study demonstrates that incorporating radiative cooling in wind-multicloud simulations explains the multiphase nature of galactic winds and enhances the effectiveness of hydrodynamic shielding. A multiphase gas forms, where regions of cold, dense gas coexist with warm and hot, low-density gas. In addition, shielding increases the lifetime of cold clouds and preserves dense material, albeit at the cost of reducing its velocity. Future research should consider incorporating additional physical processes to further enhance our understanding of multicloud system dynamics and hydrodynamic shielding. The inclusion of magnetic fields, self-gravity, and electron thermal conduction can provide valuable insights into how these factors influence dense gas survival.

## ACKNOWLEDGEMENTS

The authors gratefully acknowledge the Gauss Centre for Supercomputing e.V. ([www.gauss-centre.eu](http://www.gauss-centre.eu)) for funding this project by providing computing time (via grant pn34qu) on the GCS Supercomputer SuperMUC-NG at the Leibniz Supercomputing Centre ([www.lrz.de](http://www.lrz.de)). In addition, the authors thank CEDIA ([www.cedia.edu.ec](http://www.cedia.edu.ec)) for providing access to their HPC cluster as well as technical support. This work has made use of the VISIT visualization software (Childs et al. 2012). We also thank the developers of the PLUTO code for making this hydrodynamic code available to the community. WEBB is supported by the National Secretariat of Higher Education, Science, Technology, and Innovation of Ecuador, SENESCYT.

## DATA AVAILABILITY

The data underlying this article will be shared on reasonable request to the corresponding authors.

## REFERENCES

- Abruzzo M. W., Fielding D. B., Bryan G. L., 2022, arXiv e-prints, p. [arXiv:2210.15679](https://arxiv.org/abs/2210.15679)
- Alüzas R., Pittard J. M., Hartquist T. W., Falle S. A. E. G., Langton R., 2012, *MNRAS*, **425**, 2212
- Banda-Barragán W. E., Parkin E. R., Federrath C., Crocker R. M., Bicknell G. V., 2016, *MNRAS*, **455**, 1309
- Banda-Barragán W. E., Federrath C., Crocker R. M., Bicknell G. V., 2018, *MNRAS*, **473**, 3454
- Banda-Barragán W. E., Zertuche F. J., Federrath C., García Del Valle J., Brüggen M., Wagner A. Y., 2019, *MNRAS*, **486**, 4526
- Banda-Barragán W. E., Brüggen M., Federrath C., Wagner A. Y., Scannapieco E., Cottle J., 2020, *Monthly Notices of the Royal Astronomical Society*, **499**, 2173
- Banda-Barragán W. E., Brüggen M., Heesen V., Scannapieco E., Cottle J., Federrath C., Wagner A. Y., 2021, *Monthly Notices of the Royal Astronomical Society*, **506**, 5658
- Borthakur S., et al., 2015, *ApJ*, **813**, 46
- Brüggen M., Scannapieco E., 2016, *ApJ*, **822**, 31
- Casavecchia B., Banda-Barragán W. E., Brüggen M., Brightenti F., 2023, *IAU Symposium*, **362**, 56
- Chevalier R. A., Clegg A. W., 1985, *Nature*, **317**, 44

- Childs H., et al., 2012, in , High Performance Visualization—Enabling Extreme-Scale Scientific Insight. "Lawrence Berkeley National Laboratory Scientific Data", pp 357–372
- Choi W., Kim C.-G., Chung A., 2022, *ApJ*, **936**, 133
- Cooper J. L., Bicknell G. V., Sutherland R. S., Bland-Hawthorn J., 2008, *ApJ*, **674**, 157
- Cooper J. L., Bicknell G. V., Sutherland R. S., Bland-Hawthorn J., 2009, *ApJ*, **703**, 330
- Cottle J., Scannapieco E., Brüggen M., Banda-Barragán W., Federrath C., 2020, *ApJ*, **892**, 59
- Di Teodoro E. M., McClure-Griffiths N. M., Lockman F. J., Armillotta L., 2020, *Nature*, **584**, 364
- Faucher-Giguère C.-A., Oh S. P., 2023, *ARA&A*, **61**, 131
- Ferland G. J., Korista K. T., Verner D. A., Ferguson J. W., Kingdon J. B., Verner E. M., 1998, *PASP*, **110**, 761
- Fielding D. B., Ostriker E. C., Bryan G. L., Jermyn A. S., 2020, *ApJ*, **894**, L24
- Forbes J. C., Lin D. N. C., 2019, *The Astronomical Journal*, **158**, 124
- Fragile P. C., Murray S. D., Anninos P., van Breugel W., 2004, *ApJ*, **604**, 74
- Goldsmith K. J. A., Pittard J. M., 2017, *MNRAS*, **470**, 2427
- Gregori G., Miniati F., Ryu D., Jones T. W., 2000, *The Astrophysical Journal*, **543**, 775
- Gronke M., Oh S. P., 2018, *MNRAS*, **480**, L111
- Gronke M., Oh S. P., 2020, *MNRAS*, **492**, 1970
- Gronke M., Oh S. P., Ji S., Norman C., 2022, *MNRAS*, **511**, 859
- Heyer M., et al., 2022, *The Astrophysical Journal*, **930**, 170
- Ji S., Oh S. P., Masterson P., 2019, *MNRAS*, **487**, 737
- Jung S. L., Grønnow A., McClure-Griffiths N. M., 2023, *MNRAS*, **522**, 4161
- Kanjilal V., Dutta A., Sharma P., 2021, *MNRAS*, **501**, 1143
- Kim C.-G., et al., 2020, *ApJ*, **903**, L34
- Klein R. I., McKee C. F., Colella P., 1994, *ApJ*, **420**, 213
- Levy R. C., et al., 2023, *arXiv e-prints*, p. arXiv:2309.15906
- Li Z., Hopkins P. F., Squire J., Hummels C., 2020, *MNRAS*, **492**, 1841
- Li F., et al., 2022, *ApJ*, **933**, 139
- Marinacci F., Binney J., Fraternali F., Nipoti C., Ciotti L., Londrillo P., 2010, *MNRAS*, **404**, 1464
- McClure-Griffiths N. M., Green J. A., Hill A. S., Lockman F. J., Dickey J. M., Gaensler B. M., Green A. J., 2013, *ApJ*, **770**, L4
- McClure-Griffiths N. M., et al., 2018, *Nature Astronomy*, **2**, 901
- McCourt M., Oh S. P., O’Leary R., Madigan A.-M., 2018, *MNRAS*, **473**, 5407
- McPherson D. K., et al., 2023, *MNRAS*, **525**, 6170
- Mignone A., 2014, *Journal of Computational Physics*, **270**, 784
- Mignone A., Bodo G., Massaglia S., Matsakos T., Tesileanu O., Zanni C., Ferrari A., 2007, *The Astrophysical Journal Supplement Series*, **170**, 228
- Murray S. D., White S. D. M., Blondin J. M., Lin D. N. C., 1993, *ApJ*, **407**, 588
- Nakamura F., McKee C. F., Klein R. I., Fisher R. T., 2006, *The Astrophysical Journal Supplement Series*, **164**, 477
- Pfuhl O., et al., 2015, *ApJ*, **798**, 111
- Pittard J. M., 2022, *MNRAS*, **515**, 1815
- Pittard J. M., Parkin E. R., 2016, *MNRAS*, **457**, 4470
- Ponti G., Morris M. R., Churazov E., Heywood I., Fender R. P., 2021, *A&A*, **646**, A66
- Rathjen T.-E., Naab T., Walch S., Seifried D., Girichidis P., Wünsch R., 2023, *MNRAS*, **522**, 1843
- Reichardt Chu B., et al., 2022, *ApJ*, **941**, 163
- Roberts-Borsani G. W., Saintonge A., Masters K. L., Stark D. V., 2020, *MNRAS*, **493**, 3081
- Rubin K. H. R., et al., 2022, *ApJ*, **936**, 171
- Rupke D., 2018, *Galaxies*, **6**, 138
- Salak D., Tomiyasu Y., Nakai N., Kuno N., Miyamoto Y., Kaneko H., 2018, *The Astrophysical Journal*, **856**, 97
- Scannapieco E., Brüggen M., 2015, *ApJ*, **805**, 158
- Schneider E. E., Robertson B. E., 2017, *ApJ*, **834**, 144
- Schneider E. E., Robertson B. E., Thompson T. A., 2018, *ApJ*, **862**, 56
- Schneider E. E., Ostriker E. C., Robertson B. E., Thompson T. A., 2020, *ApJ*, **895**, 43
- Shopbell P. L., Bland-Hawthorn J., 1998, *The Astrophysical Journal*, **493**, 129
- Sparre M., Pfrommer C., Ehlert K., 2020, *MNRAS*, **499**, 4261
- Strickland D. K., Stevens I. R., 2000, *MNRAS*, **314**, 511
- Tchernyshyov K., et al., 2022, *ApJ*, **927**, 147
- Teşileanu O., Mignone A., Massaglia S., 2008, *A&A*, **488**, 429
- Teodoro E. M. D., McClure-Griffiths N. M., Lockman F. J., Denbo S. R., Endsley R., Ford H. A., Harrington K., 2018, *The Astrophysical Journal*, **855**, 33
- Toro E. F., Spruce M., Speares W., 1994, *Shock waves*, **4**, 25
- Tripp T. M., et al., 2011, *Science*, **334**, 952
- Tumlinson J., et al., 2011, *Science*, **334**, 948
- Veilleux S., Rupke D. S. N., Swaters R., 2009, *ApJ*, **700**, L149
- Veilleux S., Maiolino R., Bolatto A. D., Aalto S., 2020, *A&ARv*, **28**, 2
- Veilleux S., et al., 2021, *MNRAS*, **508**, 4902
- Westmoquette M. S., Smith L. J., Gallagher J. S., 2008, *MNRAS*, **383**, 864
- Xu J., Stone J. M., 1995, *ApJ*, **454**, 172
- Zhang D., Thompson T. A., Quataert E., Murray N., 2017, *MNRAS*, **468**, 4801
- Zhang M., Li Z., Morris M. R., 2021, *ApJ*, **913**, 68

## APPENDIX A: SOME EXTRA MATERIAL

The panels of Figure A1 show the steady-state wind solution for the CC85 model as a function of distance from the central starburst. The intersection between the dimensionless parameters and the red vertical dashed lines ( $\text{Log10}(r^*) = 0.3$ ) represent the initial conditions chosen for the simulations (see Section 2.3).

This paper has been typeset from a *TeX/LaTeX* file prepared by the author.

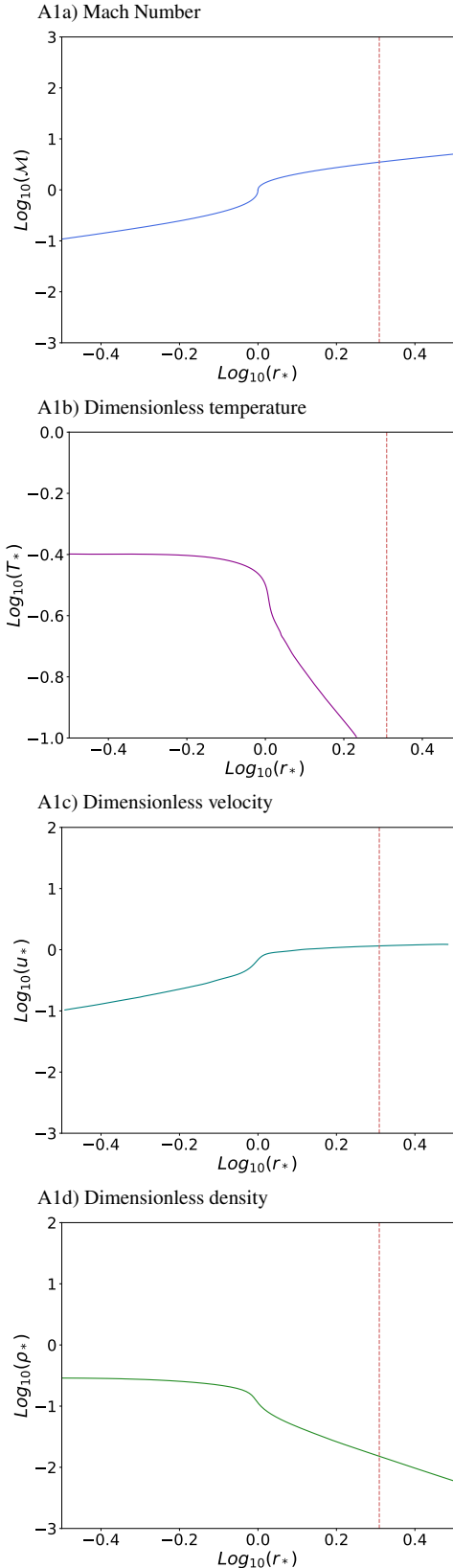


**Figure A1.** Analytical Solutions for the CC85 model of Mach number (panel A1a), dimensionless temperature (panel A1b), dimensionless velocity (panel A1c), and dimensionless density (panel A1d).